Supplementary Information (SI) for Catalysis Science & Technology.

Supporting Information

Halide-Guided Carbon-Affinity Active Site in $Bi_mO_nBr_p$-Derived $Bi_2O_2CO_3$ for Efficient Electrocatalytic CO_2 Reduction to Formate

Dengye Yang[a], Qing Mao[*, a], Yuting Feng[a], Wei Zhou[a]

[a] *School of Chemical Engineering, Dalian University of Technology, Dalian 116024, China*

[*]Corresponding Author

E-mail: maoqing@dlut.edu.cn

Table of Contents

1 Product analysis

1.1 Gas product analysis

Gas chromatography (GC, Techcomp, GC7900) equipped with a flame ionization detector (FID) and a thermal conductivity detector (TCD) was used to qualitatively and quantitatively determine the gaseous products (such as H_2 and CO or other gaseous hydrocarbons).

$$FE = \frac{Q_g}{Q_{total}} = \frac{n \cdot Z \cdot F}{Q_{total}} \times 100\% = \frac{V\% \cdot \nu \cdot z \cdot F}{I_{average} \cdot V_m} \times 100\% \qquad \text{(Eq. S1)}$$

Where V % is the relative content of gas product, υ is CO_2 flow rate (40 sccm), z is the electron transfer number (z = 2, 2, 8, and 12 for H_2, CO, CH_4, and C_2H_4, respectively), F is the Faraday constant (96485 $C \cdot mol^{-1}$), V_m is the gas molar volume (22.4 $L \cdot mol^{-1}$ under standard conditions), $I_{average}$ is the total steady-state current density ($mA \cdot cm^{-2}$).

1.2 Liquid product analysis

Liquid products were detected by 1H nuclear magnetic resonance spectroscopy (1H NMR). In the 1H NMR spectra, the peak area of products such as formate was used to quantify the concentrations of formate and other liquid products. The faradaic efficiency (FE) of the liquid product was determined as follows:

$$FE = \frac{Q_L}{Q_T} = \frac{n \cdot Z \cdot F}{Q_T} \times 100\% \qquad \text{(Eq. S2)}$$

Where n is the mole of liquid product, z is the required number of electrons (z = 2, 6, 8, 12 and 18 for formate, methanol, acetate, ethanol, and 1-propanol, respectively). F is

Faraday constant (96485 $C{\cdot}mol^{-1}$), Q_L and Q_T are the charge used to produce the liquid product and the total charge consumed in CO_2RR, respectively.

2 Kinetics calculation section of CO_2RR to formate

The kinetic parameters of the kinetic models were obtained by fitting the models with steady-state internal resistance (IR)-corrected J_{HCOO^-}-V curves using a global optimization method, which comprises a random search using genetic algorithm and a local optimization employing a trust-region reflective algorithm. All simulations were performed using a commercial software package (MATLAB R2010b, the MathWorks Inc.). The reaction rate equations and control equations are listed in Table S2. The corresponding kinetic parameters under 20 $mA\cdot cm^{-2}$ are listed in Table S3. The active site content normalized kinetic parameters under 20 $mA\cdot cm^{-2}$ are listed in Table S4.

3 Supporting Figures and Tables

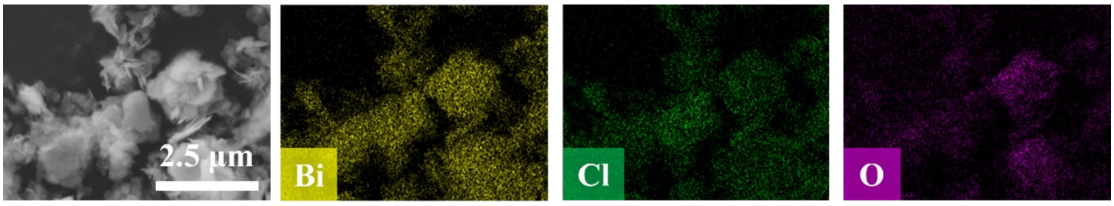

Figure. S1. The SEM image of BiOCl catalysts.

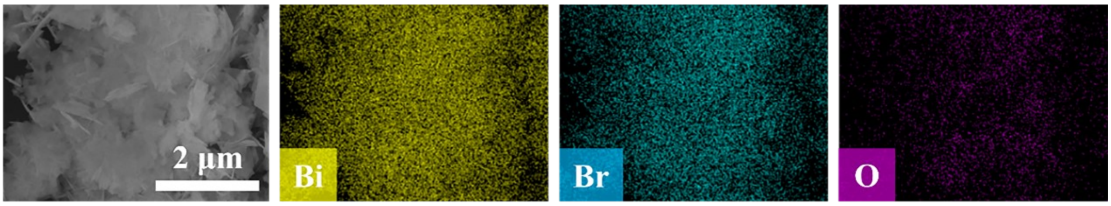

Figure. S2. The SEM image of $Bi_mO_nBr_p$ catalysts.

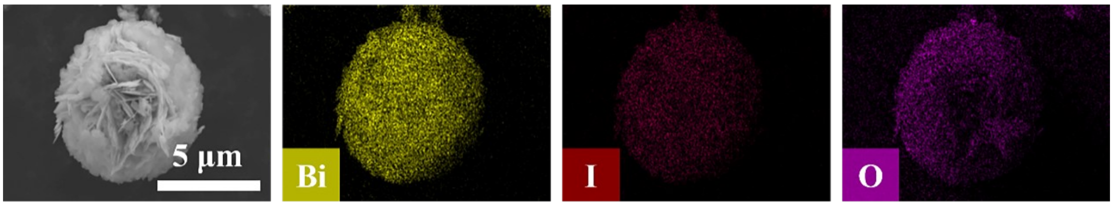

Figure. S3. The SEM image of BiOI catalysts

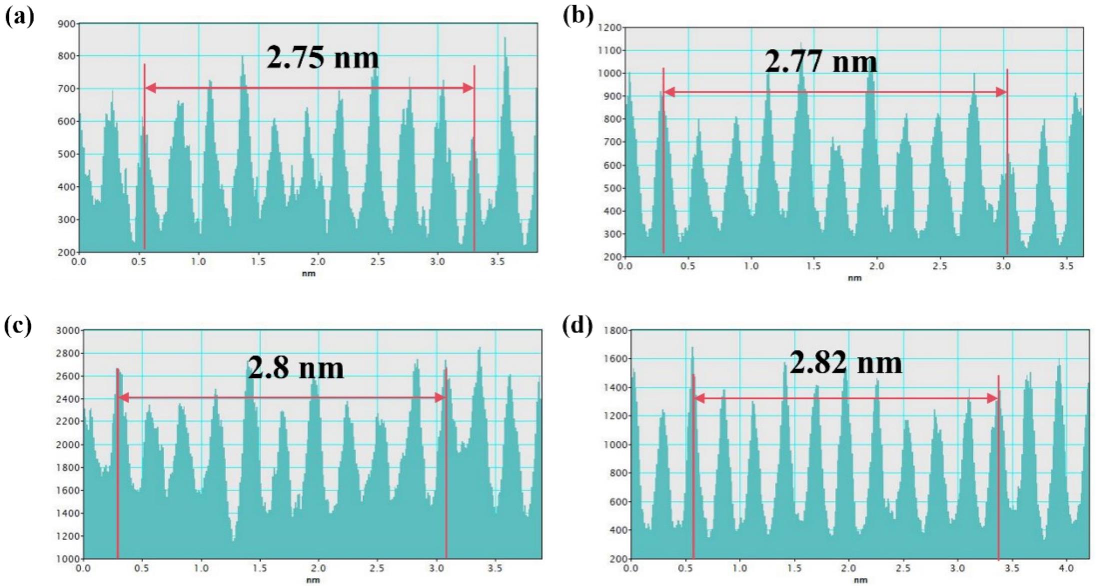

Figure. S4. The atomic intensity line scanning analysis images. (a) BiOCl, (b) BiOBr, (c) $Bi_{24}O_{31}Br_{10}$ and (d) BiOI catalyst

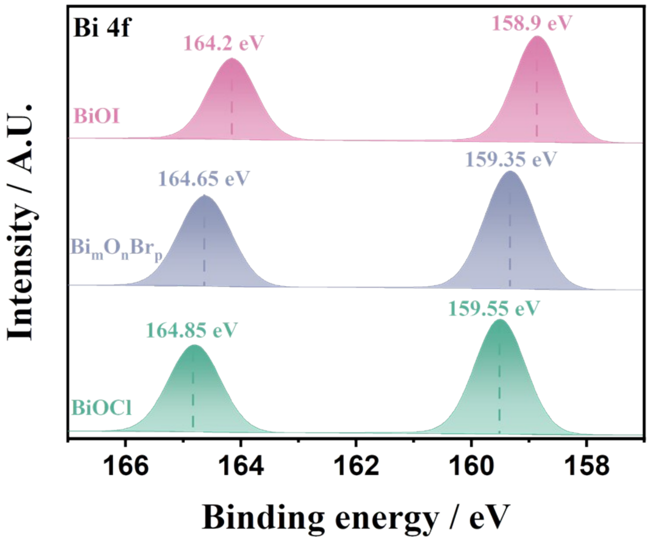

Figure. S5. The XPS Bi 4f spectrum of BiOCl, $Bi_mO_nBr_p$ and BiOI.

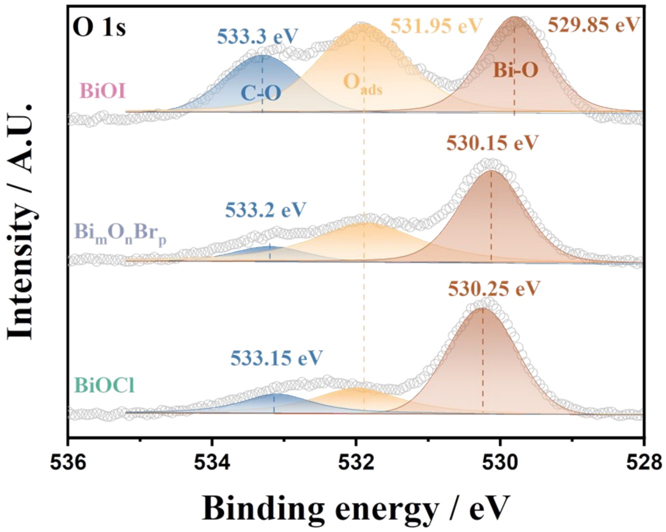

Figure. S6. The XPS O 1s spectrum of BiOCl, $Bi_mO_nBr_p$ and BiOI. The peaks were assigned to Bi-O structure (529.85 ~ 530.25 eV)[1], O_{ads} (531.95 eV)[2] and C-O structure (533.15 ~ 533.3 eV). The C-O signal maybe come from formation of $Bi_2O_2CO_3$ reaction with CO_2 in the air. The content result was listed in Table S1.

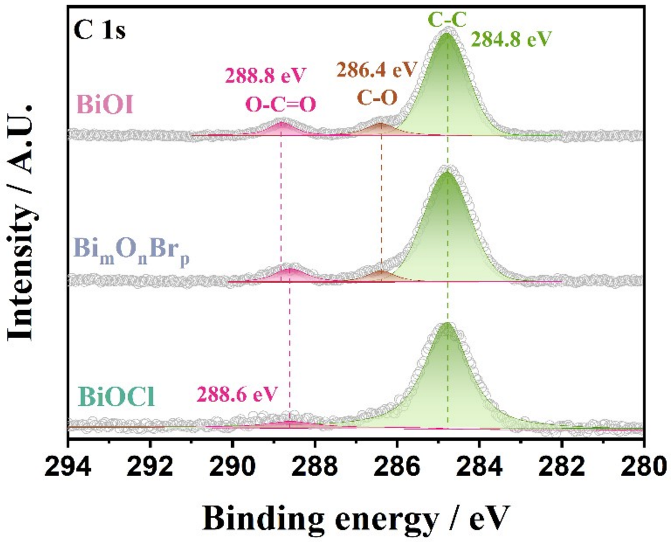

Figure. S7. The XPS C 1s spectrum of BiOCl, $Bi_mO_nBr_p$ and BiOI. The peaks were assigned to carbon in nature (284.8 eV), C-O structure (286.4 eV)[3] and O-C=O structure (288.6 ~ 288.8 eV). The C-O and O-C=O signal maybe come from formation of $Bi_2O_2CO_3$ reaction with CO_2 in the air. The content result was listed in Table S2.

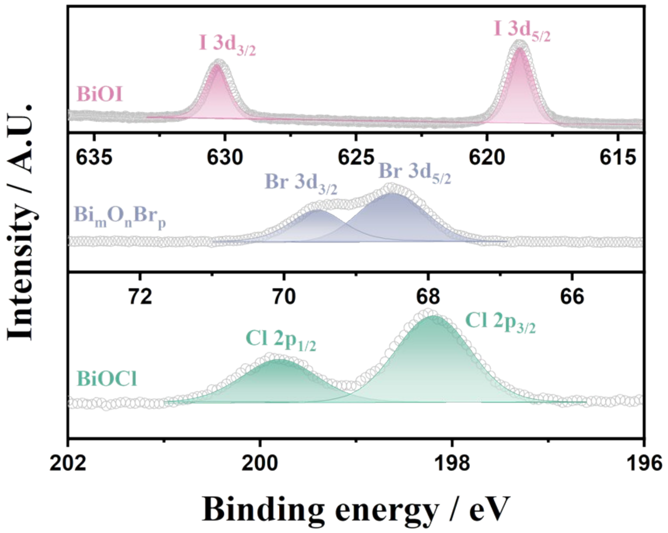

Figure. S8. The XPS Cl, Br, I spectra of BiOCl, $Bi_mO_nBr_p$ and BiOI.

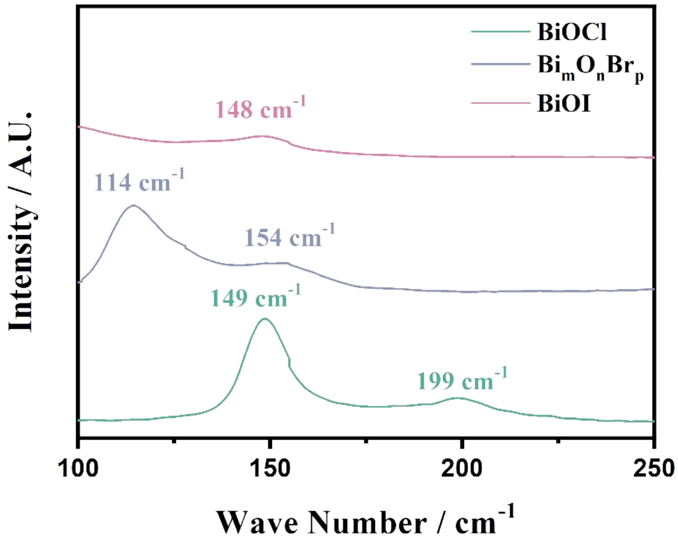

Figure. S9. The Raman spectra of BiOCl, $Bi_mO_nBr_p$ and BiOI. In Raman spectra, the peaks at 149 cm^{-1} and 199 cm^{-1} can be assigned to A_{1g} internal Bi-Cl stretching mode and E_g internal Bi-Cl stretching mode[4]; those at 114 cm^{-1} and 154 cm^{-1} can be assigned to A_{1g} internal Bi-Br stretching mode and E_g internal Bi-Br stretching mode[5]; the characteristic Raman peak of BiOI locates at 148 cm^{-1}[6, 7].

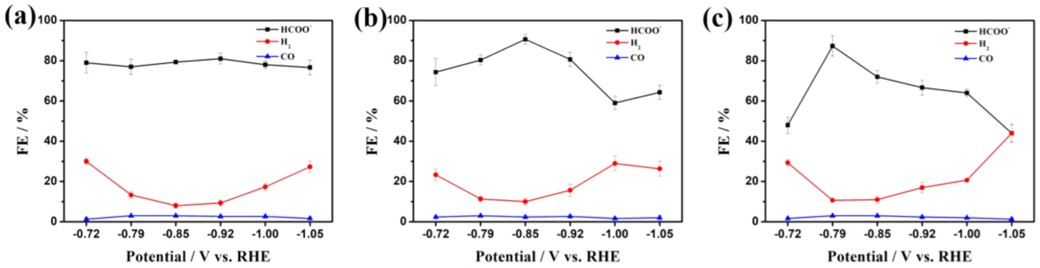

Figure. S10. The BiOX Faradic efficiency of formate, H_2 and CO during CO_2RR from -0.72 V to -1.05 V vs. RHE of (a) BiOCl, (b) $Bi_mO_nBr_p$ and (c) BiOI.

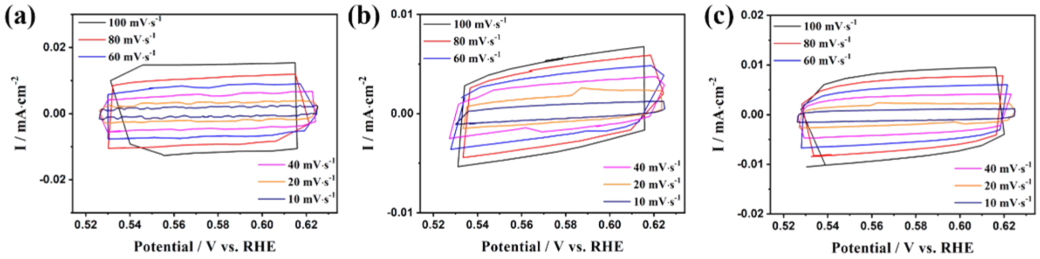

Figure. S11. The CV curves of the BiOX catalysts during ECSA test from 100 mV·s^{-1} to 10 mV·s^{-1}. (a) BiOCl, (b) $Bi_mO_nBr_p$ and (c) BiOI.

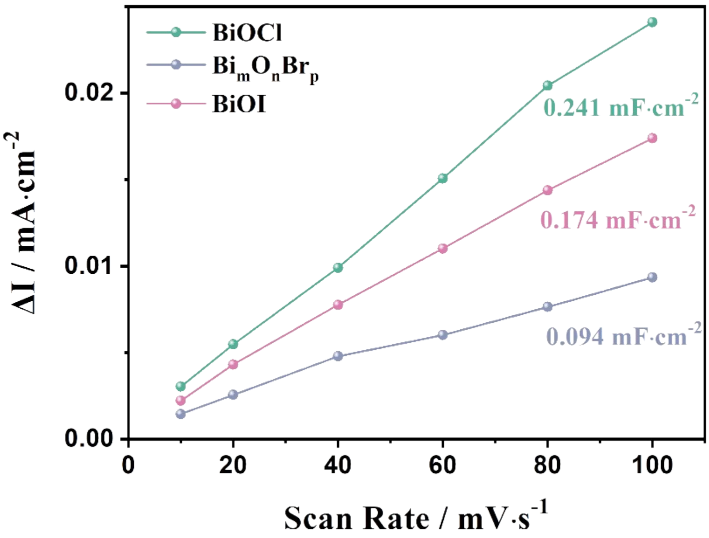

Figure. S12. The C_{dl} value of BiOCl, $Bi_mO_nBr_p$ and BiOI. $Bi_mO_nBr_p$ has the lowest C_{dl} (0.094 mF·cm^{-2}) compared with BiOCl (0.241 mF·cm^{-2}) and BiOI (0.174 mF·cm^{-2}), support that $Bi_mO_nBr_p$ high performance is attributed to the feature of active sites rather than the number of the active sites.

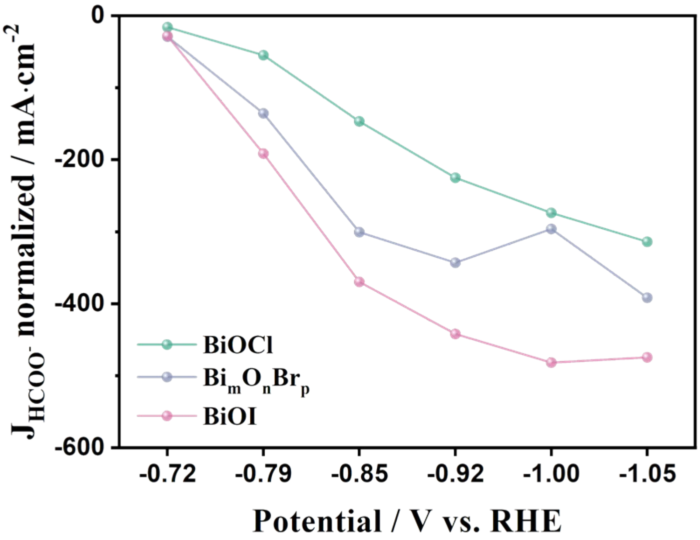

Figure. S13. The C_{dl} normalized formate partial current density of BiOCl, $Bi_mO_nBr_p$ and BiOI. BiOI has the largest normalized J_{HCOO^-}, which means that BiOI has the most

CO_2RR active sites density. The $Bi_mO_nBr_p$ anomalous J_{HCOO^-} decrease in 1.0 V (vs. RHE) observed here is a common phenomenon during electrode selectivity test on Bi-based catalysts. Numerous publications have mentioned a sudden decrease in formic acid faradaic efficiency at around -1.0 V vs. RHE[7, 8]. Therefore, the phenomenon observed in this paper is normal, and its underlying mechanism is expected to be further explored by subsequent researchers.

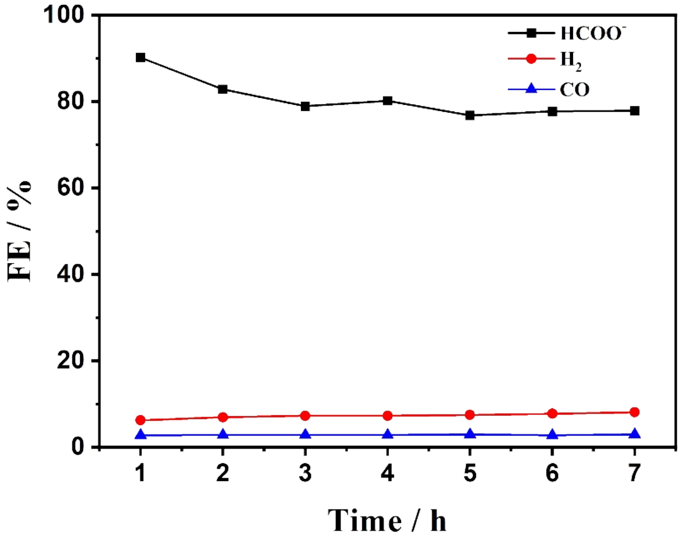

Figure. S14. The $Bi_mO_nBr_p$ FE of formate, H_2 and CO generation during the 7h CO_2RR stability test.

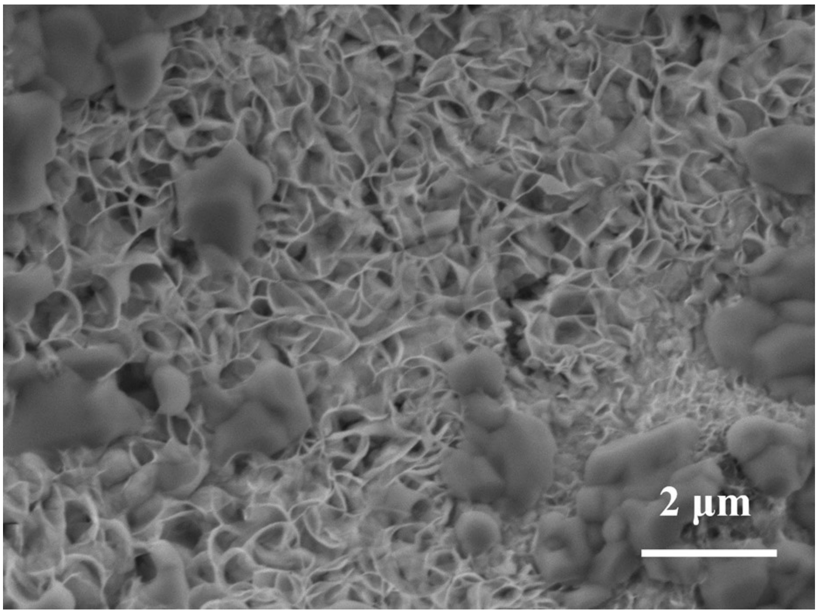

Figure. S15. The SEM image of $Bi_mO_nBr_p$ after 7 hours electrolysis

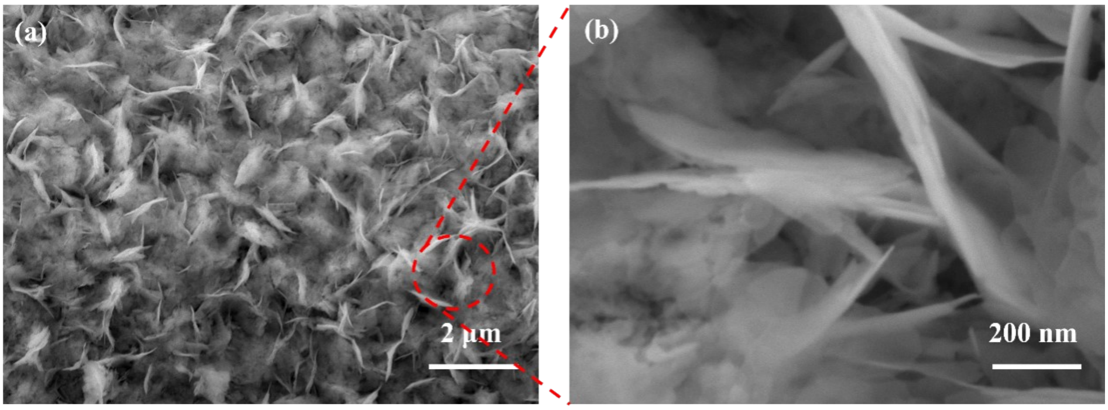

Figure. S16. The SEM image of $Bi_mO_nBr_p$ after 1 hour electrolysis. (a) The SEM image of electrode surface. (b) The SEM image of electrode surface under high magnification.

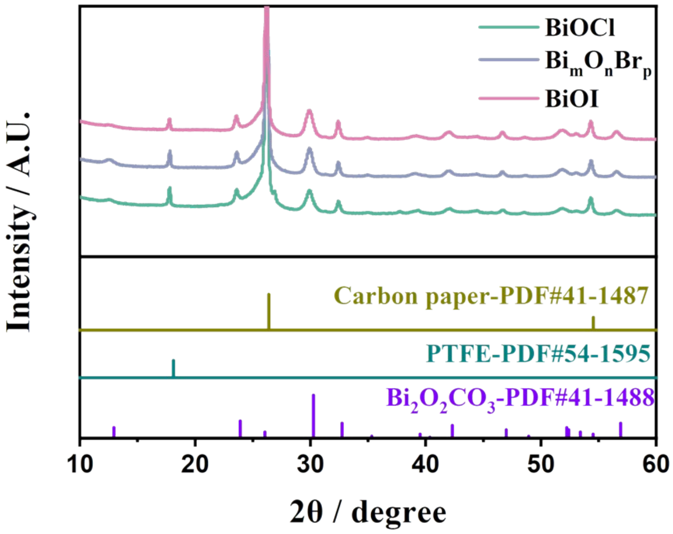

Figure. S17. The XRD pattern of BiOCl, $Bi_mO_nBr_p$ and BiOI after CO_2RR.

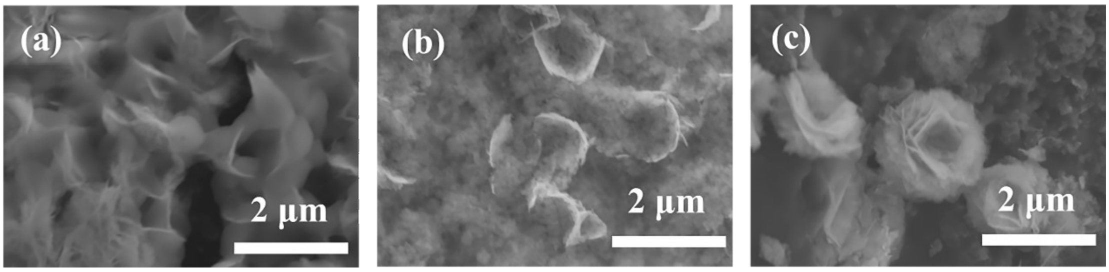

Figure. S18. The SEM images of (a) BiOCl, (b) $Bi_mO_nBr_p$ and (c) BiOI after CO_2RR.

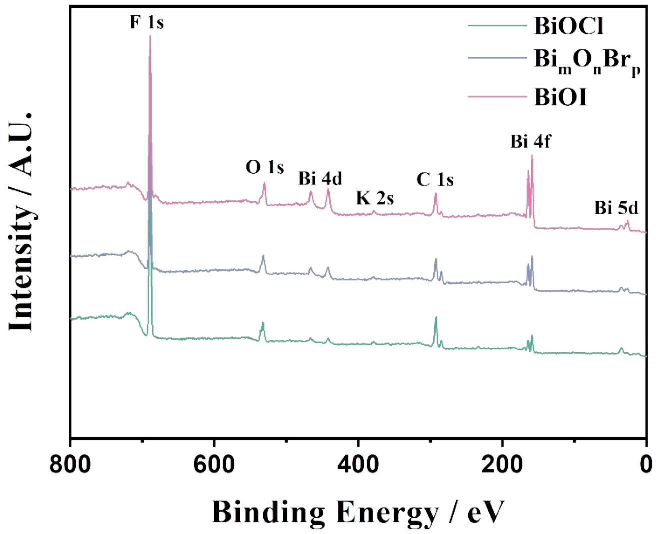

Figure. S19. The XPS total spectra of $Bi_mO_nX_p$-derived $Bi_2O_2CO_3$ catalysts after CO_2RR.

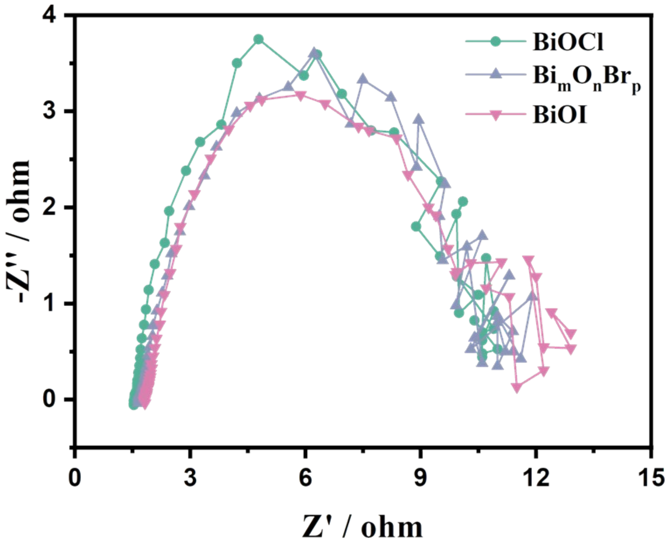

Figure. S20. The EIS test results of BiOCl, $Bi_mO_nBr_p$ and BiOI from 0.1 Hz to 20000 Hz. The Internal Resistance is 1.48 Ω of BiOCl, 1.64 Ω of $Bi_mO_nBr_p$ and 1.55 Ω of BiOI.

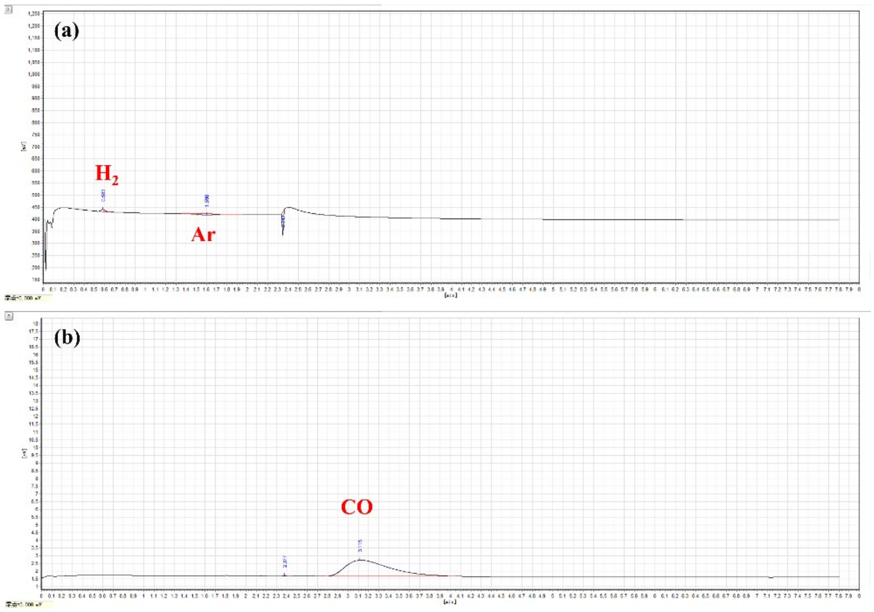

Figure. S21. The gas chromatographic spectra of $Bi_mO_nBr_p$ during CO_2RR stability test. (a) TCD spectrum, (b) FID spectrum. The H_2 and CO are only two gas products.

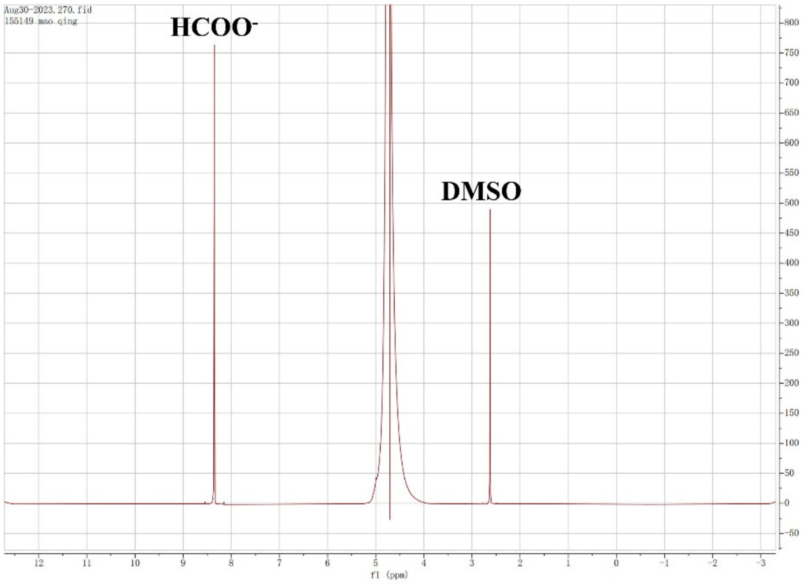

Figure. S22. The ^{1}H-NMR spectrum of $Bi_mO_nBr_p$ during CO_2RR stability test. The $HCOO^-$ is the only one liquid product.

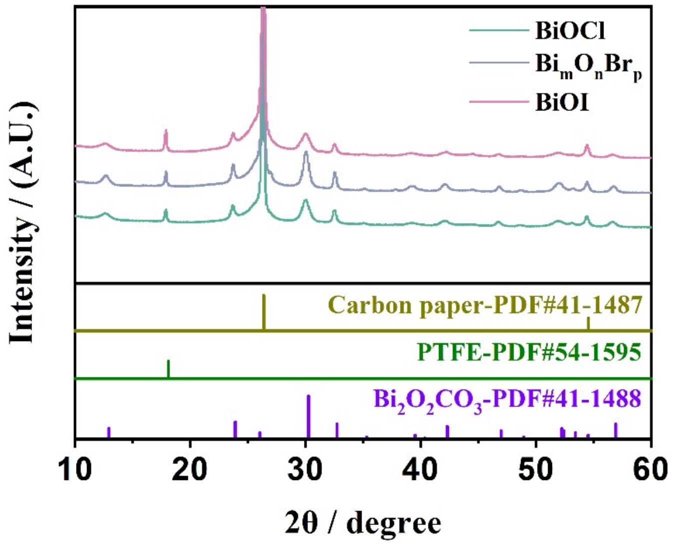

Figure. S23. The XRD pattern of BiOCl, $Bi_mO_nBr_p$ and BiOI after CV activation.

Table S1. The XPS O 1s content results of $Bi_mO_nX_p$ before CO_2RR.

	Bi-O / %	O_{ads} / %	C-O / %
BiOCl	59.64	24.87	15.49
$Bi_mO_nBr_p$	49.66	41.66	8.68
BiOI	34.26	45.02	20.72

Table S2. The XPS C 1s content results of $Bi_mO_nX_p$ before CO_2RR.

	C-C / %	O-C=O / %	C-O / %
BiOCl	94.31	5.69	0
$Bi_mO_nBr_p$	82.87	7.13	10.00
BiOI	82.45	9.13	8.42

Table S3. Reaction rate equations and control equations for CO_2RR to formate.

Kinetic equations for the elementary steps of CO_2RR

$$r_1 = K_{101} \cdot (1 - \theta_{CO_{2,ads}} - \theta_{COOH_{ads}}) \cdot (\frac{P_{CO_2}}{P^{\Theta}}) \tag{Eq. S1}$$

$$r_{-1} = K_{102} \cdot \theta_{CO_{2,ads}} \tag{Eq. S2}$$

$$r_2 = K_{201} \cdot \theta_{CO_{2,ads}} \cdot (\frac{C_{CO_2}}{C^{\Theta}}) \cdot exp(\frac{\alpha F\eta}{RT}) \tag{Eq. S3}$$

$$r_{-2} = K_{201} \cdot \theta_{COOH_{ads}} \cdot (\frac{C_{HCO_3^-}}{C^{\Theta}}) \cdot exp(-\frac{(1-\alpha)F\eta}{RT}) \tag{Eq. S4}$$

$$r_3 = K_{301} \cdot \theta_{COOH_{ads}} \cdot exp(-\frac{\alpha F\eta}{RT}) \tag{Eq. S5}$$

$$r_{-3} = K_{301} \cdot (1 - \theta_{CO_{2,ads}} - \theta_{COOH_{ads}}) \cdot (\frac{C_{HCOO^-}}{C^{\Theta}}) \cdot exp(-\frac{(1-\alpha)F\eta}{RT}) \tag{Eq. S6}$$

Control equations for the CO_2RR process

$$C_{CO_{2,ads}} \frac{dq_{CO_2}}{dt} = r_1 - r_{-1} - r_2 + r_{-2} \tag{Eq. S7}$$

$$C_{COOH_{ads}} \frac{d\theta_{COOH}}{dt} = r_2 - r_{-2} - r_3 + r_{-3} \tag{Eq. S8}$$

$$C_{dl} \frac{dE}{dt} = j(t) - [(r_2 - r_{-2}) + (r_3 - r_{-3})] \cdot F/n \tag{Eq. S9}$$

Note: Where r is the elementary reaction rate ($mol \cdot m^{-2} \cdot s^{-1}$), K is the reaction rate constant ($mol \cdot m^{-2} \cdot s^{-1}$), c is the concentration ($mol \cdot m^{-3}$), θ is the coverage, α is the symmetry coefficient, η is the overpotential (V), R is the gas constant ($J \cdot mol^{-1} \cdot K^{-1}$), T is the temperature (K), θ which subscripts CO_2 and COOH represent the intermediate CO_2, ads and COOH, ads, respectively, and c which subscripts CO_2 and HCO_3^-

represent the reactant CO_2 and electrolyte $KHCO_3$, respectively.

Table S4. The rate constants under 20 mA·cm^{-2} for the elementary steps of CO_2RR on the BiOCl, $Bi_mO_nBr_p$ and BiOI-derived $Bi_2O_2CO_3$ catalysts.

Rate Constants	BiOCl	$Bi_mO_nBr_p$	BiOI
K_{101}	1.22×10^{-1}	2.62×10^{-1}	1.60×10^{-1}
K_{102}	3.93×10^{1}	3.27×10^{-2}	7.12×10^{-2}
$K_{201} \cdot exp(\frac{\alpha F\eta}{RT})$	3.66×10^{-7}	1.52×10^{-9}	3.53×10^{-9}
$K_{202} \cdot exp(-\frac{(1-\alpha)F\eta}{RT})$	5.25×10^{-9}	8.71×10^{-10}	3.01×10^{-10}
$K_{301} \cdot exp(\frac{\alpha F\eta}{RT})$	8.27×10^{-5}	2.24×10^{-5}	5.67×10^{-6}
$K_{302} \cdot exp(-\frac{(1-\alpha)F\eta}{RT})$	7.98×10^{-4}	4.15×10^{-3}	2.31×10^{-3}

Table S5. The active site normalized content rate constants under 20 mA·cm^{-2} for the elementary steps of CO_2RR on the BiOCl, $Bi_mO_nBr_p$ and BiOI-derived $Bi_2O_2CO_3$ catalysts.

Normalized Rate Constants	BiOCl	$Bi_mO_nBr_p$	BiOI
K_{101}/N	6.08×10^{0}	1.90×10^{1}	3.02×10^{0}
K_{102}/N	1.96×10^{3}	2.38×10^{0}	1.34×10^{0}
$K_{201}\cdot exp(\frac{\alpha F\eta}{RT})/N$	1.83×10^{-5}	1.11×10^{-7}	6.66×10^{-8}
$K_{202}\cdot exp(-\frac{(1-\alpha)F\eta}{RT})/N$	2.63×10^{-7}	6.33×10^{-8}	5.67×10^{-9}
$K_{301}\cdot exp(\frac{\alpha F\eta}{RT})/N$	4.13×10^{-3}	1.62×10^{-3}	1.07×10^{-4}
$K_{302}\cdot exp(-\frac{(1-\alpha)F\eta}{RT})/N$	3.99×10^{-2}	3.02×10^{-1}	4.36×10^{-2}

Note: Where N is the parament which represents active site content. N=Bi-O content (%) × C_{dl}. The Bi-O content were calculated by XPS O1s results after CO_2RR.

Table S6. The XPS O 1s content results of $Bi_mO_nX_p$ after CO_2RR.

	Bi-O / %	**O-C=O / %**	**O_{ads} / %**	**O-F / %**
BiOCl	**8.30**	**7.76**	**59.65**	**24.29**
$Bi_mO_nBr_p$	**14.65**	**18.20**	**51.23**	**15.92**
BiOI	**30.50**	**23.47**	**29.46**	**16.57**

Table S7. The mole fraction of Bi^{3+} dissolution of BiOCl, $Bi_mO_nBr_p$ and BiOI calculated by ICP-OES results.

	Bi^{3+} dissolution mole fraction / %
BiOCl	**3.099**
$Bi_mO_nBr_p$	**3.026**
BiOI	**2.988**

Table S8. Comparison of catalytic performances of $Bi_mO_nBr_p$ catalysts and the reported Bi-based catalysts in H-type cell when they reach at 90 % FE_{HCOO^-}

	J_{HCOO^-} / $mA \cdot cm^{-2}$	Potential / V (vs. RHE)
$Bi_mO_nBr_p$(This work)	52.31	-0.85
Bi_2O_2S[10]	32.7	-0.90
CeO_x-$Bi_2O_2CO_3$[11]	18	-1.00
BiOI microflower[12]	41.3	-1.00
Bi@$B_2O_2CO_3$[13]	20	-0.80
Bi-BTB[9]	12.70	-0.67
2D-$Bi_2O_2CO_3$[14]	3	-0.80
Bi_2O_3@C-800[15]	7.5	-0.90
$BiPO_4$[16]	17	-1.20
2D-Bi[17]	21	-0.83
In / Bi-750[18]	32.22	-1.40
Bi-TiO_2-700[19]	8.4	-1.00
Bi_5O_7I[20]	14.9	-0.89
Bi_2S_3-ppy[21]	56.95	-1.20

Reference

[1] Hu R., Xiao X., Tu S., et al. Synthesis of flower-like heterostructured β-Bi_2O_3 / $Bi_2O_2CO_3$ microspheres using $Bi_2O_2CO_3$ self-sacrifice precursor and its visible-light-induced photocatalytic degradation of o-phenylphenol[J]. Applied Catalysis B: Environmental, 2015, 163: 510-519.

[2] Xu Y., Guo Y., Sheng Y., et al. Selective CO_2 Electroreduction to Formate on Polypyrrole-Modified Oxygen Vacancy-Rich Bi_2O_3 Nanosheet Precatalysts by Local Microenvironment Modulation[J]. Small, 2023, 19(29): 2300001.

[3] Greczynski G., Hultman L. The same chemical state of carbon gives rise to two peaks in X-ray photoelectron spectroscopy[J]. Scientific Reports, 2021, 11(1): 11195.

[4] Dong F., Sun Y., Fu M., et al. Room temperature synthesis and highly enhanced visible light photocatalytic activity of porous BiOI /BiOCl composites nanoplates microflowers[J]. Journal of Hazardous Materials, 2012, 219-220: 26-34.

[5] Zhang D., Li J., Wang Q., et al. High {001} facets dominated BiOBr lamellas: facile hydrolysis preparation and selective visible-light photocatalytic activity[J]. Journal of Materials Chemistry A, 2013, 1(30): 8622-8629.

[6] Abuelwafa A. A., Matiur R. M., Putri A. A., et al. Synthesis, structure, and optical properties of the nanocrystalline bismuth oxyiodide (BiOI) for optoelectronic application[J]. Optical Materials, 2020, 109: 110413.

[7] Jiang Z., Liang X., Liu Y., et al. Enhancing visible light photocatalytic degradation performance and bactericidal activity of BiOI via ultrathin-layer structure[J]. Applied

Catalysis B: Environmental, 2017, 211: 252-257.

[8] Fu H. Q., Liu J., Bedford N. M., et al. Operando Converting BiOCl into $Bi_2O_2(CO_3)_xCl_y$ for Efficient Electrocatalytic Reduction of Carbon Dioxide to Formate[J]. Nano-Micro Letters, 2022, 14(1): 121.

[9] Yuan W.-W., Wu J.-X., Zhang X.-D., et al. In situ transformation of bismuth metal–organic frameworks for efficient selective electroreduction of CO_2 to formate[J]. Journal of Materials Chemistry A, 2020, 8(46): 24486-24492.

[10] Liu S., Wang T., Liu X., et al. In Situ Dissociated Chalcogenide Anions Regulate the Bi-Catalyst / Electrolyte Interface with Accelerated Surface Reconstruction toward Efficient CO_2 Reduction[J]. ACS Catalysis, 2024, 14(1): 489-497.

[11] He A., Wang C., Zhang N., et al. Oxygen vacancy-rich CeO_x-$Bi_2O_2CO_3$ nanosheets for enhancing electrocatalytic reduction of CO_2 to formate[J]. Applied Surface Science, 2023, 638: 158140.

[12] Liu P. F., Zu M. Y., Zheng L. R., et al. Bismuth oxyiodide microflower-derived catalysts for efficient CO_2 electroreduction in a wide negative potential region[J]. Chemical Communications, 2019, 55(82): 12392-12395.

[13] Liang X.-D., Zheng Q.-Z., Wei N., et al. In-situ constructing Bi@$Bi_2O_2CO_3$ nanosheet catalyst for ampere-level CO_2 electroreduction to formate[J]. Nano Energy, 2023, 114: 108638.

[14] Cho W. S., Hong D. M., Dong W. J., et al. Porously Reduced 2-Dimensional $Bi_2O_2CO_3$ Petals for Strain-Mediated Electrochemical CO2 Reduction to HCOOH[J]. Energy & Environmental Materials, 2024, 7(1): e12490.

[15] Deng P., Yang F., Wang Z., et al. Metal–Organic Framework-Derived Carbon Nanorods Encapsulating Bismuth Oxides for Rapid and Selective CO_2 Electroreduction to Formate[J]. Angewandte Chemie International Edition, 2020, 59(27): 10807-10813.

[16] Fan T., Ma W., Xie M., et al. Achieving high current density for electrocatalytic reduction of CO_2 to formate on bismuth-based catalysts[J]. Cell Reports Physical Science, 2021, 2(3): 100353.

[17] Yang S., Jiang M., Zhang W., et al. In Situ Structure Refactoring of Bismuth Nanoflowers for Highly Selective Electrochemical Reduction of CO_2 to Formate[J]. Advanced Functional Materials, 2023, 33(37).

[18] Wang Q., Yang X., Zang H., et al. InBi Bimetallic Sites for Efficient Electrochemical Reduction of CO_2 to HCOOH[J]. Small, 2023, 19(41).

[19] Jia G., Wang Y., Sun M., et al. Size Effects of Highly Dispersed Bismuth Nanoparticles on Electrocatalytic Reduction of Carbon Dioxide to Formic Acid[J]. Journal of the American Chemical Society, 2023, 145(25): 14133-14142.

[20] Wang Q., Ma M., Zhang S., et al. Influence of the Chemical Compositions of Bismuth Oxyiodides on the Electroreduction of Carbon Dioxide to Formate[J]. ChemPlusChem, 2020, 85(4): 672-678.

[21] Li C., Liu Z., Zhou X., et al. Bio-inspired engineering of Bi_2S_3–PPy composite for the efficient electrocatalytic reduction of carbon dioxide[J]. Energy & Environmental Science, 2023, 16(9): 3885-3898.